Article

Author for correspondence:
A. Malin Johansson,
E-mail: malin.johansson@uit.no

Consistent ice and open water classification combining historical synthetic aperture radar satellite images from ERS-1/2, Envisat ASAR, RADARSAT-2 and Sentinel-1A/B

A. Malin Johansson[1] ![ORCID], Eirik Malnes[2], Sebastian Gerland[3], Anca Cristea[1], Anthony P. Doulgeris[1], Dmitry V. Divine[3], Olga Pavlova[3] and Tom Rune Lauknes[2]

[1]UiT The Arctic University of Norway, Tromsø, Norway; [2]NORCE Norwegian Research Centre AS, Tromsø, Norway and [3]Norwegian Polar Institute, Tromsø, Norway

Abstract

Synthetic Aperture Radar (SAR) satellite images are used to monitor Arctic sea ice, with systematic data records dating back to 1991. We propose a semi-supervised classification method that separates open water from sea ice and can utilise ERS-1/2, Envisat ASAR, RADARSAT-2 and Sentinel-1 SAR images. The classification combines automatic segmentation with a manual segment selection stage. The segmentation algorithm requires only the backscatter intensities and incidence angle values as input, therefore can be used to establish a consistent decadal sea ice record. In this study we investigate the sea ice conditions in two Svalbard fjords, Kongsfjorden and Rijpfjorden. Both fjords have a seasonal ice cover, though Rijpfjorden has a longer sea ice season. The satellite image dataset has weekly to daily records from 2002 until now, and less frequent records between 1991 and 2002. Time overlap between different sensors is investigated to ensure consistency in the reported sea ice cover. The classification results have been compared to high-resolution SAR data as well as in-situ measurements and sea ice maps from Ny-Ålesund. For both fjords the length of the sea ice season has shortened since 2002 and for Kongsfjorden the maximum sea ice coverage is significantly lower after 2006.

1. Introduction

Sea ice is a key parameter in controlling heat, gas and light exchange between the atmosphere and the ocean. Since 1981 the Arctic Ocean has lost ∼11% of its sea ice area per decade (Fetterer and others, 2019). The largest observed changes occur in the winter months, December–February (Screen and Simmonds, 2010), and the area north of Svalbard has experienced a 10% sea ice reduction per decade for the months of December–March (Onarheim and others, 2014). More localised studies on Svalbard by Muckenhuber and others (2016) found that the maximum fast ice area, for two westward facing fjords, had reduced with 23.2 and 35.2% respectively. Increased sea water temperatures have been found to affect the sea ice location and extent (Lind and others, 2018). These changes affect, among other things, the ecosystems that depend on the presence of sea ice (e.g. Arrigo and van Dijken, 2015; Leu and others, 2016; Assmy and others, 2017). Increased monitoring, including comparison to historical records of the sea ice cover and its subsequent changes in winter months, is therefore essential for tracking trends over time.

Satellite data offer the possibility to monitor large areas with a high temporal resolution, e.g. on a daily basis. By using satellite images, investigations of reduced sea ice cover (Stroeve and others, 2012), thinning sea ice (Giles and others, 2008; Kwok and Cunningham, 2015; Lindsay and Schweiger, 2015) and extended melt ice season are possible (Stroeve and others, 2014; Bliss and others, 2017). Synthetic aperture radar (SAR) satellite images are visibility and daylight independent, and therefore suitable for monitoring the Arctic Ocean where both weather conditions, such as fog and clouds, and the polar night limit monitoring by, e.g. optical sensors. SAR images have been acquired over the Arctic since Seasat in 1978, though consistent monitoring started with ERS-1 in 1992. Since 2002, near semi-weekly to daily SAR coverage of the Arctic region is possible, and the constellation of Sentinel-1 (S-1) satellites is expected to be operational until 2040, permitting studies of the seasonal evolution with respect to fractional ice cover and length of the season (Muckenhuber and others, 2016). A challenge for decadal seasonality studies is how to establish consistent and transferable methods that can employ SAR data from a range of different satellite sensors, and where the data records facilitate inter-calibration between different sensors (Eisenman and others, 2014).

We propose a generic classification method where we manually separate open water and sea ice segments that were obtained by automatic segmentation for two Svalbard fjords; Kongsfjorden and Rijpfjorden. For this we use a long time series of SAR images, starting with ERS-1 and ending with S-1. Near-daily monitoring of the fjord ice is possible using Envisat ASAR Wide swath (2002–12), RADARSAT-2 ScanSAR (2012–ongoing) and Sentinel-1A/B EW (2014– ongoing) images. Overlap in time between Envisat ASAR and

![CrossMark]

Table 1. Overview of the SAR images used in this study. The ERS-1, ERS-2, Envisat ASAR and Sentinel-1A/B sensors are from the European Space Agency (ESA) and the RADARSAT-2 satellite is operated by the Canadian Space Agency (CSA) and MacDonald Dettwiler and Associates Ltd (MDA). IW stands for Interferometric Wide, EW for Extra Wide, V is vertical and H is horizontal in transmit and receive

Sensor	Mode	Channel	# of images Kongsfjorden/Rijpfjorden	Dates
ERS-1	SAR Imaging	VV	18/-	199111 to 199206
ERS-2	SAR Imaging	VV	66/-	199505 to 200206
Envisat ASAR	Wide Swath (WSM)	HH	2248/2276	200210 to 201204
Envisat ASAR	Wide Swath (WSM)	VV	154/6	200211 to 200909
RADARSAT-2	ScanSAR wide swath (SCWA)	HH/HV	151/799	201202 to 201411
Sentinel-1A and 1B	IW + EW	HH/HV	1267/1081	201410 to 201909

RADARSAT-2 and between RADARSAT-2 and S-1A/B ensures that a validation and comparison between the different sensors is possible. In order to validate our method we compare the results with in-situ observations, optical photographs, and high-resolution SAR images. We produce a decadal record of the sea ice extent, freezing onset, melt season onset and sea ice season length for two fjords on Svalbard, Kongsfjorden and Rijpfjorden.

2. Satellite data

For this study ∼4000 SAR images covering each of the two different fjords were used. The satellite dataset consists of images from six different satellite sensors, all of them C-band SAR (Table 1). ERS-1 and ERS-2 had few acquisitions due to narrow swaths and un-systematic sampling, whereas Envisat ASAR (ASAR) provided coverage twice per week on average and daily in periods. Weekly RADARSAT-2 (RS-2) images and daily S-1A/B images were used. The used polarisation channels vary with the different satellite sensors (Table 1). RS-2 and S-1A/B have a dual polarimetric setup and here the HH/HV-combination is used.

3. Study area

Kongsfjorden is located in the north-western part of Spitsbergen island, Svalbard. Inner parts of the fjord are covered by landfast and drifting sea ice in the winter and spring months, with substantial inter-annual variability with respect to timing, extent and thickness (Gerland and Renner, 2007; Pavlova and others, 2019). Kongsfjorden is dominated by young ice during winter (December–March) and by first-year fast ice in spring (April–May) (Svendsen and others, 2002). Glacier ice, in the form of icebergs and ice pieces may be frozen into the fast ice. The fjord is ∼ 27 km long, between 4 and 10 km wide, and with a total open water area of ∼220 km^2 (Torsvik and others, 2019). Five marine-terminating glaciers surround Kongsfjorden, all of them contributing glacier ice to the fjord through calving events. Kongsbreen lost a total surface of 2.5 km^2 and Kronebreen 2.8 km^2 between 2007 and 2013 (Schellenberger and others, 2015). Hence, the glacier ice generally constitutes a small portion of the total fjord ice area. Though hereafter when referring to all the ice located within the fjord we use the term fjord ice. The calving events are largely controlled by sea water temperature, and have their yearly minimum from January to May (Luckman and others, 2015; Schild and others, 2018), and this coincides with the peak in sea ice extent (Gerland and Renner, 2007). The fjord is open to the sea in the north west, and water from the West Spitsbergen Current (WSC red line in Fig. 1a) can enter the fjord through this opening (Svendsen and others, 2002).

During the time of year with daylight hours, near-daily manual ice maps are produced and web-camera images are taken from the Zeppelinfjellet (Fig. 1b) (Gerland and Renner, 2007). The manually drawn maps are complemented by regular visits to the sea ice (since 2003), along with more sporadically collected datasets since the 1980s. During the annual sea ice monitoring campaigns, sea ice thickness, snow thickness and freeboard are sampled among other parameters. Additionally, in 2016–2018 the fast ice edge was traced using a handheld GPS and a small boat (Negrel and others, 2018). Weather data are continuously collected in Ny-Ålesund and regular measurements of ocean parameters are carried out in Kongsfjorden (Cottier and others, 2019; Hop and others, 2019b). These combined data sets provide an opportunity to validate the robustness of the open water versus sea fjord classification.

Some in-situ observations exist for Rijpfjorden, e.g. water and air temperature and photographs from 2006 and onward (Cottier and others, 2019), additionally there are also data collected during shorter time periods in 2006–2007 (Howe and others, 2010; Søreide and others, 2010), 2006–2008 (Wallace and others, 2010), 2010–2014 (Hop and others, 2019a) and 2011 (Wang and others, 2013). Rijpfjorden is located at Nordaustlandet, on the Northern part of Svalbard (Fig. 1c), and is usually covered by sea ice up to 9 months of the year (Ambrose and others, 2006; Leu and others, 2011), though less sea ice and higher air and water temperatures have been recorded in recent years (Hop and others, 2019a). The fjord is north-facing and drift ice enters the fjord under the influence of northerly winds (Ambrose and others, 2006; Leu and others, 2011). The total open water area is 724 km^2. The warm Atlantic water in the WSC does not influence Rijpfjorden as much as it does Kongsfjorden (Cottier and others, 2007; Howe and others, 2010), though this may change in the future (Onarheim and others, 2014; Hop and others, 2019a).

4. Method

We propose an ice-open water classification method that supports SAR images from a range of different sensors. The SAR images are automatically segmented based on statistical properties of the data (Doulgeris and Cristea, 2018; Cristea and others, undergoing revisions), and subsequently the segments are manually classified as either open water or fjord ice. The method consists of three different steps: the pre-processing, the segmentation and the classification.

4.1. Satellite data pre-processing

All available satellite scenes were geocoded using the geocoding tool of the GSAR software (Larsen and others, 2006). Each scene is geocoded on a fixed grid using 50 m × 50 m pixel spacing, centering the images over the center point for the respective fjords. For the ASAR and RS-2 images this yields some oversampling and hence more speckle than necessary, but the advantage of a homogeneous input product was preferred. The backscatter values were radiometrically calibrated using the ESA standard protocol (Collecte Localisation Satellites, 2019). All products were stored as Geotiff images in WGS-84, UTM Z33N. In
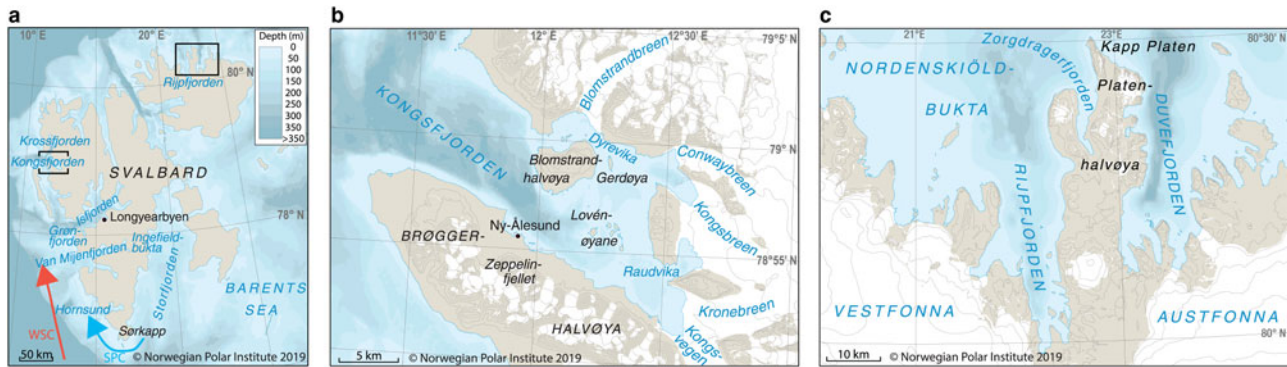
Fig. 1. (a) Map over Svalbard. The red arrow indicate the West Spitsbergen Current (WSC) and the blue arrow the Spitsbergen Polar Current (SPC). The two boxes indicate Kongsfjorden (left) and Rijpfjorden (top right), (b) Kongsfjorden and (c) Rijpfjorden. The maps are produced using digital elevation map (DEM) data from Norwegian Polar Institute (2014).

addition to the radar backscatter, the incidence angle was calculated for each pixel in order to account for variable incidence angles in the segmentation step. All images used within the study has a 100% coverage over the respective study areas.

4.2. Segmentation

The segmentation algorithm is based on a statistical model that integrates the surface-specific intensity decay rates across the satellite image. The intensity decay is due to incidence angle variation and is significant for relatively flat surfaces, such as open water and sea ice. Moreover, the decay rates depend on polarisation and surface roughness and consequently vary between ice types (e.g. Shokr, 2009; Gupta and others, 2014; Mahmud and others, 2018). If the intensity decay is not accounted for, pixels are grouped together based on intensity levels alone, even if they correspond to different physical structures (Doulgeris and Cristea, 2018; Cristea and others, undergoing revisions).

The algorithm is initialised with one segment, which is then alternately optimised and tested. Segment optimisation is performed with a traditional Expectation Maximisation (EM) algorithm, and the testing is performed with a Pearson's style goodness-of-fit (GOF) test of the model's fit to the data. The GOF test is followed by a segment split if the GOF criterion is not fulfilled, respectively a split of the least well-fitting segment in the case of multiple segments. The sequential algorithm stops at a statistically appropriate number of segments, being the lowest number that is a sufficiently good fit to the data. Groups of pixels with similar statistical properties will end up in the same segment, which may be spatially disjoint. A subsequent Markov random field (MRF)-based contextual smoothing stage completes the segmentation and improves the connectivity of the regions for simpler visual interpretation.

Only one intensity channel and the incidence angle information are required as input, though any number of polarimetric SAR intensity channels can be utilised. The advantage of this is the possibility to apply the algorithm on satellite images from different SAR sensors. As highlighted in Zakhvatkina and others (2017), separation of calm open water from smooth first year ice (FYI) is challenging due to the low backscatter returns, and wind-roughened open water is often challenging to separate from sea ice when only the HH-channel is used. Sandven and others (2008) showed that an improved separation was possible based on the reduced wind effect in the HV-channel. The HV channel was used when available, though it was often hampered by low signal to noise ratio (SNR) (in particular for the thinner sea ice types) and consequently did not always improve the segmentation substantially. For the ERS-1, ERS-2 and ASAR images

one polarisation channel was available (Table 1), and two channels were available for RS-2 and S-1.

The classification stages are presented in Figure 2a and an example from satellite image to classified scene using a RS-2 scene is shown in Figures 2b–d. As a part of the segmentation process, the images were multi-looked by 2×2 and log-transformed. Multi-looking was done to reduce the speckle and to increase the contrast and the log-transformation was done to ensure that the data is approximately Gaussian-distributed. Surrounding land areas and glaciers were masked out using a digital elevation model (DEM) (Norwegian Polar Institute, 2014). The same procedure was applied to the SAR images from the five different satellite sensors.

4.3. Classification

Following the segmentation, the segments were manually classified as either open water or fjord ice in a process similar to the one described in Muckenhuber and others (2016). The classification was performed based on user experience and the assumption that open water under calm wind conditions has low backscatter values compared to a higher backscatter from the iced areas, and that the HV-channel is less affected by wind-roughened surfaces and therefore facilitates separation between open water and sea ice.

To quantify changes in the fjord ice coverage, the freezing onset is defined as when the first ice is observed within the fjord and when the total fjord ice cover exceeds 20 km^2. The latter is used to limit the glacier ice contribution to the length of the fjord ice season (discussed further in Section 4.5). Similarly, the end of the fjord ice season (melt season onset) is defined as when the total fjord ice coverage is less than 20 km^2. The continuous sea ice season is defined as when the fjord ice coverage continuously exceeds 20 km^2 and no further break-ups occur until the melt season onset.

4.4. Validation of the classification

For cross-comparison between the different sensors, and to ensure that the produced fjord ice record is consistent, even when images from different sensors are used, temporally overlapping SAR images over Kongsfjorden were compared. Additionally, in-situ observations were compared with the classification results for both of the two different fjords.

4.4.1. SAR sensor and in-situ data comparison

In the satellite record over Kongsfjorden used in this study, there are 39 image pairs acquired with a maximum time difference of 12 h. Twenty-eight of these pairs are made up of ASAR and RS-2 images and 11 of RS-2 and S-1 images. The time difference
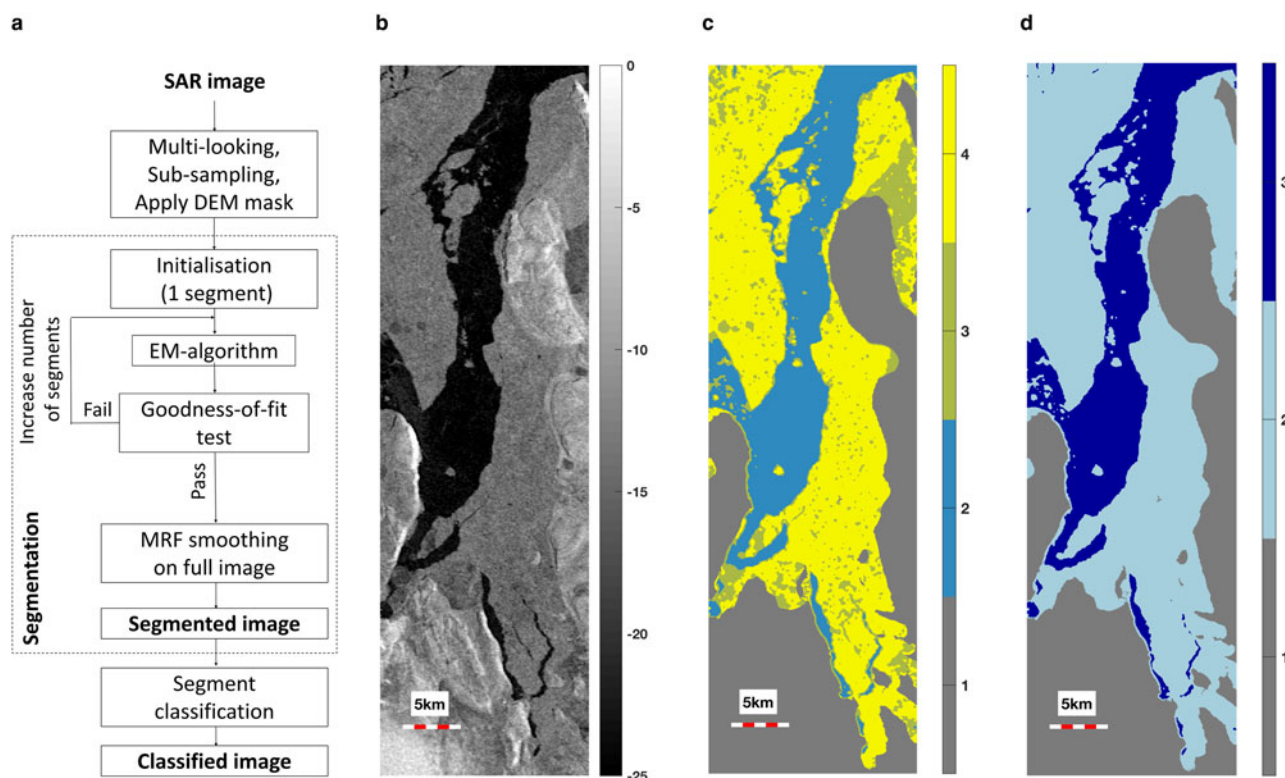
Fig. 2. (a) Flowchart outlining the different steps within the proposed method. In (b–d) illustration of the classification steps, from SAR image to classified scene is shown. (b) RADARSAT-2 HH intensity image over Rijpfjorden from 22 November 2014. The image shows backscatter intensity in dB. (c) Segmented image with three separate sea ice and open water segments and one land area segment. Segment number 1 is always the land mask. In this instance, the image was segmented into three different segments where number 3 and 4 corresponds to the fjord ice areas, whereas number 2 is the open water. (d) Classified image where grey is land, light blue is fjord ice and dark blue is open water.

restriction was used to limit the effect from sea ice drift, though the effect of potential diurnal temperature variations on the snow cover and the sea ice in itself was not eliminated, e.g. during low wind events combined with melting conditions some of the sea ice areas will have similar backscatter to the open water. Most of the RS-2 and the S-1 images were acquired in the morning, whereas the ASAR images were acquired in the afternoon.

In Figure 3 the comparison of the fjord ice area estimates is presented. The RMSE for the estimates from the RS-2 and S-1 image pairs is 7.42 and the correlation is 0.87, for the ASAR and RS-2 image pairs the RMSE is 10.8 and the correlation 0.67. Some of the area differences can be attributed to drifting sea ice and changes in the snow cover. The problem with sea ice drift over time is clearly visible south of Blomstrandhalvøya in Figure 4. The 50 m resolution S-1 EW image is acquired at 06:47 UTC and the 10 m resolution S-1 IW image is acquired at 15:44 UTC. The 10 m resolution S-1 IW image has been resampled from 5 m × 20 m resolution to 10 m × 10 m resolution. The changes in fjord ice distribution and location mean that a pixel-by-pixel comparison between the two images is not possible, and these changes are difficult to quantify without restricting investigation to the fast ice areas.

No consistent differences between the dual-polarimetric (RS-2) and single-polarimetric (ASAR) images were observed. The oversampling done on the RS-2 images may lead to less distinctive edges in these images compared to the S-1 images, though comparison between the images in each image pair indicate that the stationary ice edges have the same location in both of the images. For all image pairs the fast ice edge is generally overlapping. The accuracy of the ice edge position in the SAR sea ice maps was also confirmed with in-situ measurements carried out during annual monitoring campaigns in April 2016, May 2017 and April 2018. A hand-held GPS was used to trace the fast ice
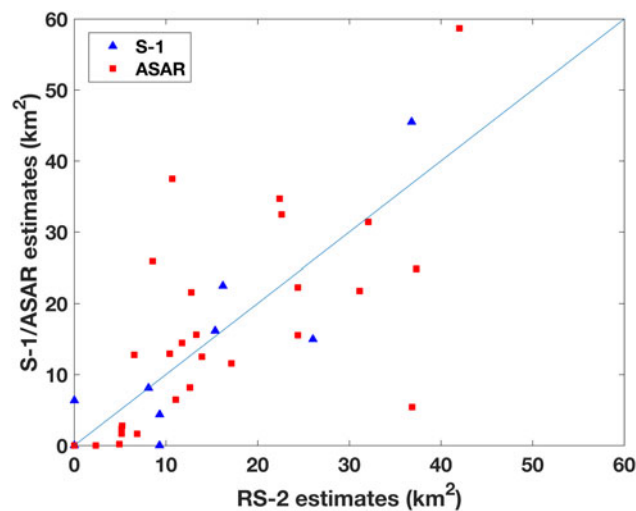

Fig. 3. Comparison between fjord ice area estimates in ASAR/RS-2 and RS-2/S-1.

edge (Negrel and others, 2018), where the GPS had a spatial sampling rate of 20 m and a precision better than 10 m (Garmin, 2011). Sea ice thickness measurements from the three campaigns indicate that the classification method can correctly identify the ice edge when the ice thickness is larger than 10 cm; sea ice being equal to or less than 10 cm thick is usually classified as open water. The GPS track from 18 April 2018 is shown as the red lines in Figures 4a–d, and here the ice thickness at the fast ice edge was 30–35 cm with a 5–9 cm thick snow layer.

Diurnal effects were noticed in one of the RS-2 and S-1 image pairs, separated by 9 h. For that day, the mean air temperature in Ny-Ålesund was $-3.5\,°C$ and at the time of the acquisition $-3.3\,°C$ (S-1) and $-1.9\,°C$ (RS-2). In-situ observations from the fast ice
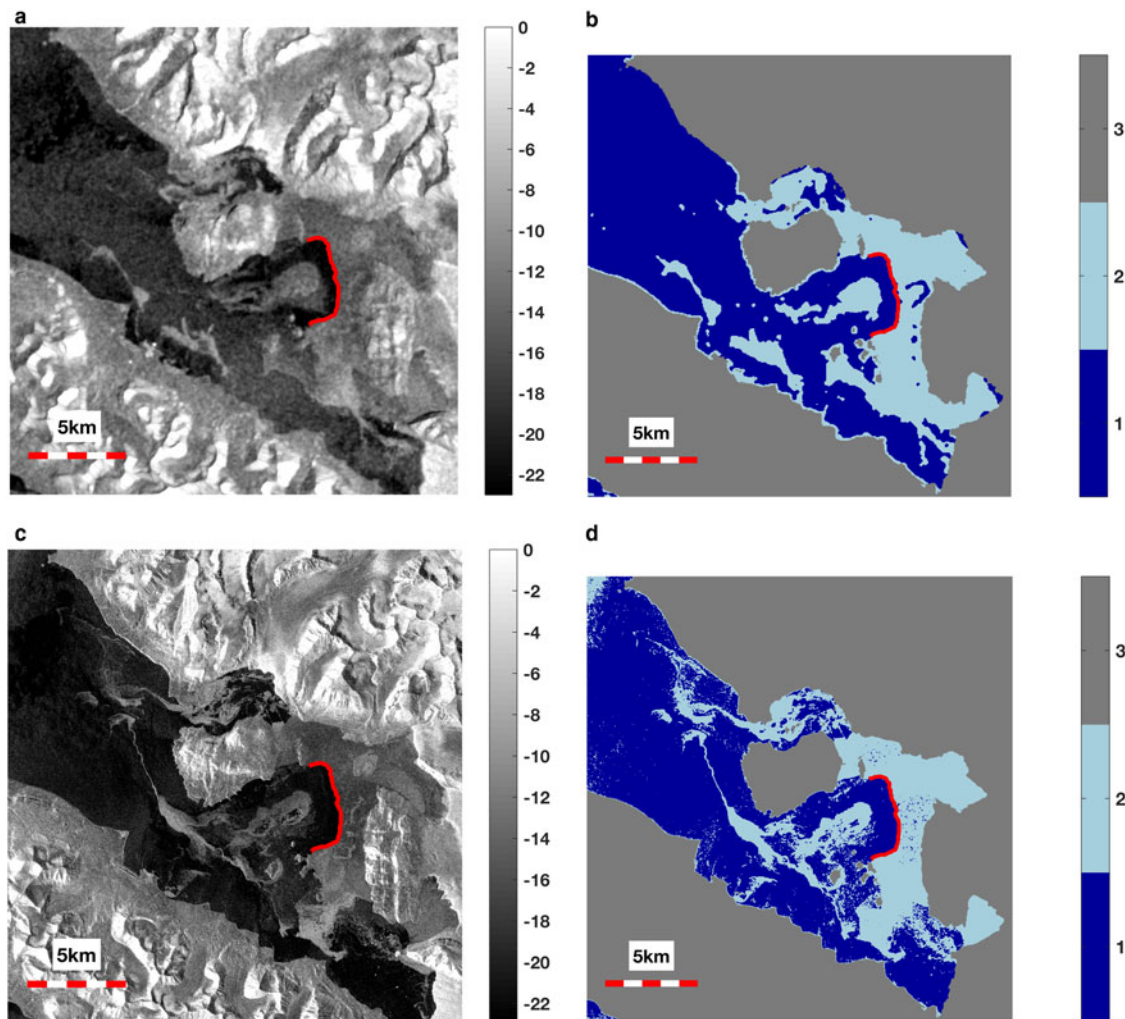
Fig. 4. S-1 backscatter HH intensity images in dB over Kongsfjorden acquired on 18 April 2018 with (a) 50 m pixel spacing in EW mode at 06:47 UTC and (c) 10 m pixel spacing in IW mode at 15:44 UTC. The classification results are shown in (b) and (d) respectively. The open water areas are dark blue (1), the fjord ice areas are light blue (2) and land areas are dark grey (3). The red line in all the images is the mapped sea ice edge on 19 April 2018 from 18:06 UTC to 18:40 UTC.

show the snow–ice interface temperature to be $-1.4°$C and water temperatures to be $-1.3°$C. It is conceivable that the sea ice experienced melting during the day and the surface layer may be wet. The wet surface will make the sea ice more similar to the open water. This can be observed in Figure 4b where a horseshoe-shaped open water area is located within the fast ice area. Nevertheless, the comparable fjord ice extent observed using satellite data from different sensors indicates that a fjord ice data record can be made using the proposed method.

4.4.2. SAR classification and manual maps comparison
In Figure 5 the ice maps produced using the SAR images are compared with the manually drawn maps from the Zeppelin mountain (Gerland and Renner, 2007; Pavlova and others, 2019). In the manually drawn maps the ice is classified as fast ice and other ice, where the latter is either sea ice that has broken off from the fast ice, thin newly formed sea ice or glacier ice. In 2018 all ice types are included in the fjord ice area estimates, and for the years before 2018 only the fast ice areas are included (Pavlova and others, 2019). The correlation between the manually drawn maps and the SAR fjord ice extent is 0.87 for 2018 and the RMSE is 16.7. For the time period from 2014 to 2018 the correlation is 0.70 and the RMSE is 20.1.

Slight time differences between the maps may affect the correlation, as the fjord ice could have drifted during the time period. Moreover, there is a slight inherent difference between the
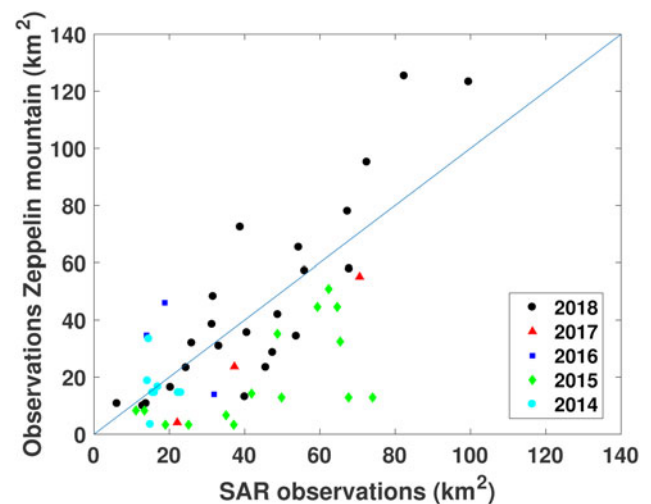

Fig. 5. The total sea ice area estimates from the Zeppelin mountain (Pavlova and others, 2019) are shown versus the total fjord ice area estimates from the proposed SAR satellite image-based method (see text).

maps, as the angular view from the Zeppelin mountain means that the inner part of Raudvika, the inner part of the fjord outside Kongsbreen and Conwaybreen and the area behind the Blomstrandhalvøya are not visible (Fig. 1b). Raudvika is the
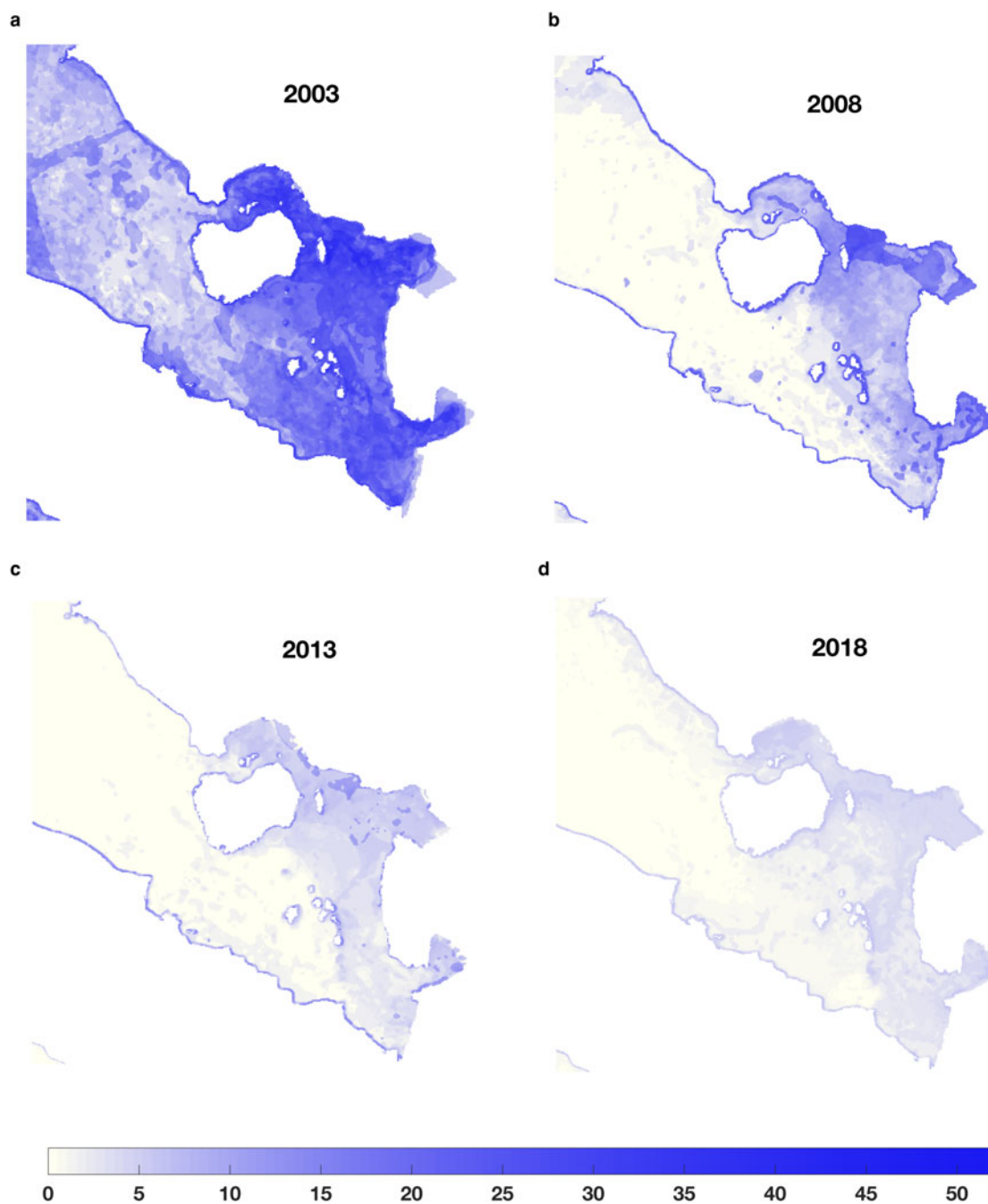
Fig. 6. Maps showing the number of weeks/year where fjord ice is observed for each satellite pixel in Kongsfjorden for (a) 2003, (b) 2008, (c) 2013 and (d) 2018. A value of 52 means that during every week of the year there was fjord ice on this exact location, whereas a value of zero means that no fjord ice was present during any of the weeks.

area where the sea ice forms first and lasts the longest (Torsvik and others, 2019). As seen in Figure 6 these areas are also the preferred location for sea ice growth. Discrepancies between the two types of maps may therefore be due to the preferred locations for sea ice growth. In Figures 6a–d the number of weeks with fjord ice coverage is shown for four different years; 2003, 2008, 2013 and 2018. The low frequency of occurrence outside Kongsbreen, Conwaybreen and Kronebreen in 2003 (Fig. 6a) is due to the fact that the marine-terminating glaciers then extended further out. High values east of Gerdøya in 2003 are explained both by a long fast ice season as well as the contribution of glacier ice during the summer months. High values in Raudvika are a consequence of the early stable fast ice formation (Torsvik and others, 2019). Exclusion of these inner areas of Kongsfjorden in the manually drawn maps may

therefore miss the start of the freezing season as well as the end of the freezing season.

From the validation we conclude that there is a good agreement between the SAR derived fjord ice areas and other independent fjord ice area estimates, and that our proposed method delivers reliable fjord ice area estimates, provided that the sea ice is not thinner than 10 cm.

4.5. Potential limitations with the method

The proposed method does not separate icebergs and glacier ice from sea ice as they often have comparable backscatter values. Kongsfjorden's five marine-terminating glaciers all calve into the fjord, and the inclusion of glacier ice may therefore lead to an overestimation of the fjord ice surface area and the length of
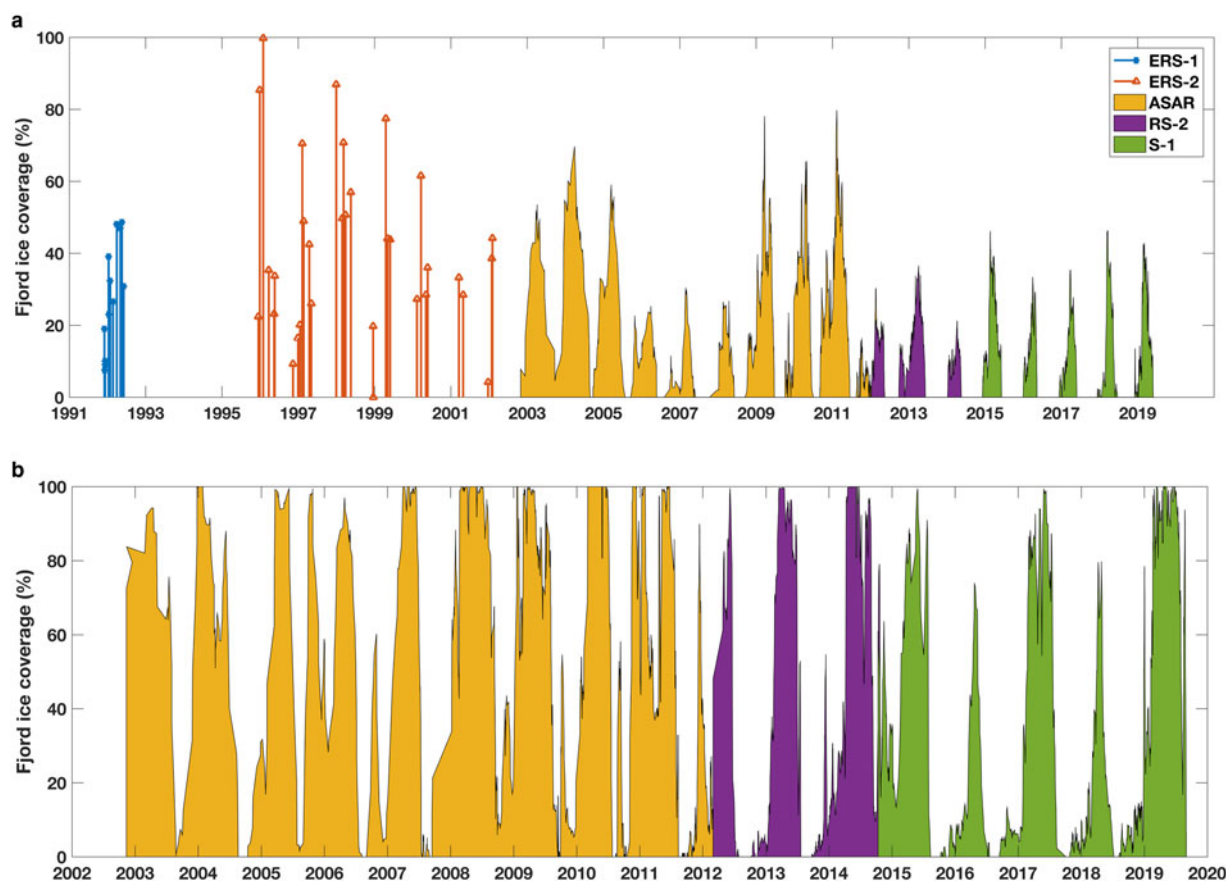
Fig. 7. Surface fjord ice coverage (in %) for (a) Kongsfjorden between 1991 and 2019 and (b) Rijpfjorden between 2002 and 2019. Data from the different sensors are marked with different colours. For ERS-1 and ERS-2 the data coverage is not continuous and stem plots are used to indicate the fjord ice coverage for those sensors, whereas ASAR, RS-2 and S-1 have at least twice weekly coverage.

the fjord ice season. However, the maximum frontal ablation rate for Kronebreen, one of these marine-terminating glaciers and also one with the highest flux rates on Svalbard, measured by Luckman and others (2015) was 8 m/day, and with an approximate width of 3 km the total ablation area for one day would be 0.02 km². Note that for the months of December–May the ablation rate was on average 4 m/day or less (Luckman and others, 2015). The total area lost during 2011 was found to be 2.8 km² (Schellenberger and others, 2015), and compared to fast ice areas in the range of up to 220 km², constitutes less than 1.3% of the total area. The glacial ice area contribution is therefore expected to be small compared to the sea ice area estimates, and the separation in time between the peak calving rate (Luckman and others, 2015) and the sea ice maximum (Gerland and Renner, 2007) implies that the glacial contribution to the total fjord ice area estimates is limited. Under some conditions, e.g. icebergs situated in calm open water during cold conditions, it may be possible to separate the two as the icebergs have higher volume scattering than the surroundings. However, separation may be hampered by the pixel resolution of the SAR images, as the effective pixel resolution after multi-looking is 100 m × 100 m and Dowdeswell and Forsberg (1992) found that few icebergs in Kongsfjorden are larger than 20 m in length. Therefore, to avoid biasing the length of the freezing season we use the continuous fjord ice season. Additionally, the fjord ice cover must be >20 km² to count towards the length of the continuous fjord ice season. We suggest that the glacier ice contribution to the fjord ice cover is limited, though inclusion of glacier ice within the fjord ice cover estimates cannot be ruled out. Further investigations where the glacier calving rates are incorporated into the fjord ice area estimates would be useful, particularly

when assessing the seasonality and the differences between different years.

The glacier ice may contribute to the evolution of the fjord ice though, as melting occurs first around icebergs and freshwater ice and these areas are hot-spots for the early fast ice break-up (Svendsen and others, 2002). Surface melting, low wind speed events and thin ice all lower the backscatter values and thereby reduce the contrast to the open water areas. Combined, these three phenomena make the fjord ice classification more challenging, and this is difficult to address without improved signal-to-noise ratio for the satellite sensors. With the present sensor configurations, sea ice thickness measurements temporally overlapping SAR classification maps indicate that when the sea ice is less than 10 cm thick it was not possible to accurately classify the ice edge. The difficulty in distinguishing the newly formed sea ice may impact the accuracy in identifying the start of the fjord ice season.

5. Results and discussion

Based on the method presented in Section 4, we have established a robust and validated fjord ice record for two fjords on Svalbard. The advantage of using daily SAR images is that the freezing onset and the break-up for the season can be captured with high spatial and temporal resolution, and that the record is independent of daylight and weather. The total fjord ice area estimates, for Kongsfjorden and Rijpfjorden, versus time are shown in Figure 7. The fjord ice seasons from 2002/03 and onward are captured in their entirety. Before 2002, the satellite coverage is sparse and estimates for the length of the freezing season are more uncertain. Significant fluctuations in the length of the
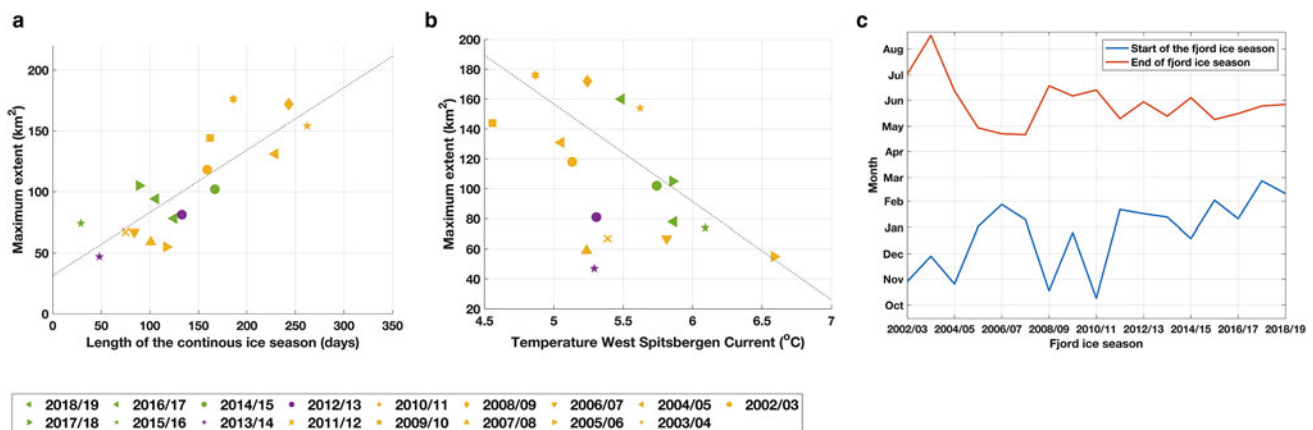
Fig. 8. The maximum surface area extent for Kongsfjorden is plotted versus (a) the length of the continuous fjord ice season and (b) the West Spitsbergen Current mean temperature. A continuous season means the time period when the fjord had a continuous fjord ice cover >20 km². The legend refers to the respective fjord ice seasons. (c) Show the start and the end of the respective fjord ice seasons for Kongsfjorden.

fjord ice season (Figs. 8a and c), the start and end of the freezing season (Fig. 8c) as well as the extent of the fjord ice cover can be observed for both fjords.

In Figure 8c we observe that the timing of the end of the fjord ice season in Kongsfjorden has some fluctuations between years, though by and large the fjord ice breaks up in May–June. However, a trend towards later fjord ice formation can be observed, where at the start of the time series the fjord ice formation took place in November–December and for the last years in February, a shift of ~2.5 months. For Kongsfjorden the fluctuations between years show a similar pattern to the ice cover estimates for Isfjorden reported in Muckenhuber and others (2016). They observed that for Isfjorden the years 2006–08 and 2012–14 had shorter sea ice seasons, as indicated by the low number of fast ice days (<20 days). For Kongsfjorden these years correspond to shorter continuous fjord ice seasons (<133 days) whereas the years 2009–2011 have longer continuous sea ice seasons (>160 days) (Fig. 8a). Moreover, the years 2006–08 and 2012–14 have lower maximum fjord ice area coverage for both Kongsfjorden (<100 km²) and Isfjorden. It is not possible to compare the length of the seasons before 2006 as the record in Muckenhuber and others (2016) then relied on optical images and the start of the seasons were not covered due to lack of daylight. This further highlights the need for consistent records relying on daylight-independent methods. Moreover, the use of a continuous SAR dataset means that image change-detection analysis may be used to distinguish the fast ice and the drifting sea ice.

The daily SAR image acquisitions means that a high degree of details about the fjord ice season can be captured. We observe that the years 2003–05 have more stable sea ice conditions and lower break-up frequency at the start of the freezing season (Fig. 9). The stability can be observed by the fact that once the ice has formed the changes in relative coverage are gradual rather than rapid (smoother transitions in the colour scale), whereas after 2008 the changes in relative coverage occur on shorter time scales and thereby lead to a higher break-up frequency. The latter can be observed in the more stripy appearance in Figure 9, implying that the fjord ice may not be stable enough to ensure continuous thickening of the sea ice. Sea ice thickness measurements in Kongsfjorden from 1997 to 2016 show that the sea ice season of 2003/04 has the thickest observed sea ice (Gerland and Renner, 2007; Pavlova and others, 2019). In Figure 8a and c we show a reduced length of the continuous fjord ice season since the start of the century, possibly as a consequence of thinner sea ice that may be more susceptible to break-up. The correlation

between the length of the continuous fjord ice season and the maximum fjord ice area is 0.83. Estimates about the break-up frequency can therefore be used to infer information about sea ice thickness.

In Figure 9 the shift in time of the year for the sea ice formation and maximum can be observed for Kongsfjorden and Rijpfjorden. This correlates well with observations for Isfjorden and Hornsund by Muckenhuber and others (2016), where they argue that the increased sea water temperature is responsible for the delayed fast ice maximum. This is similar to findings in Nilsen and others (2016), who argue that increased amounts of warm Atlantic water in the winter months affect the total fjord ice cover. We found that warmer temperatures recorded in the WSC (Norwegian Polar Institute, 2019) corresponded to a reduced maximum fjord ice extent also in Kongsfjorden (Fig. 8b) and the correlation between the water temperature and the fjord ice extent is 0.64. Summers with below average water temperatures followed by long cold winters, e.g. 2003/04, 2004/05 and 2010/11 (Cottier and others, 2019), correlate with longer fjord ice seasons with larger areal coverage (Fig. 8). Winters with above-average water temperatures during the coldest months (March–May, Cottier and others, 2019), e.g. 2005/06–2007/08, 2011/12 and 2013/14, are correlated with below-average fjord ice extent as observed in (Tverberg and others, 2019) and Figure 8b. Such a clear trend is not observed in Rijpfjorden (Cottier and others, 2019): though the winter with the warmest sea water temperatures (2016/17) also had the shortest fjord ice season and lower fjord ice extent, Figure 9b.

An eastward shift of the warmer Atlantic water has reduced the amount of drifting sea ice in December–March in the northeastern part of Svalbard (Onarheim and others, 2014), including Rijpfjorden, where there is an increased winter sea ice loss (Isaksen and others, 2016; Hop and others, 2019a). A reduction in sea ice thickness within the eastern Eurasian Basin has also been observed by Polyakov and others (2017) and has been attributed to increased water temperatures due to the eastward shift of the warmer Atlantic water. Our observations indicate that since the fjord ice season 2012/13, there has been less abundant fjord ice in Rijpfjorden in December–March, with a consistent sea ice coverage not establishing itself until February. The exception to this is the fjord ice season of 2014/15, and this year was in Cottier and others (2019) reported to have below average sea water temperatures in Rijpfjorden during September–November. Moreover, years with a delayed start of the fjord ice season, e.g. 2004/05, 2012/13 and 2015/16 (Fig. 9b), were in Lind and others (2018) shown to be years with lower sea ice import between
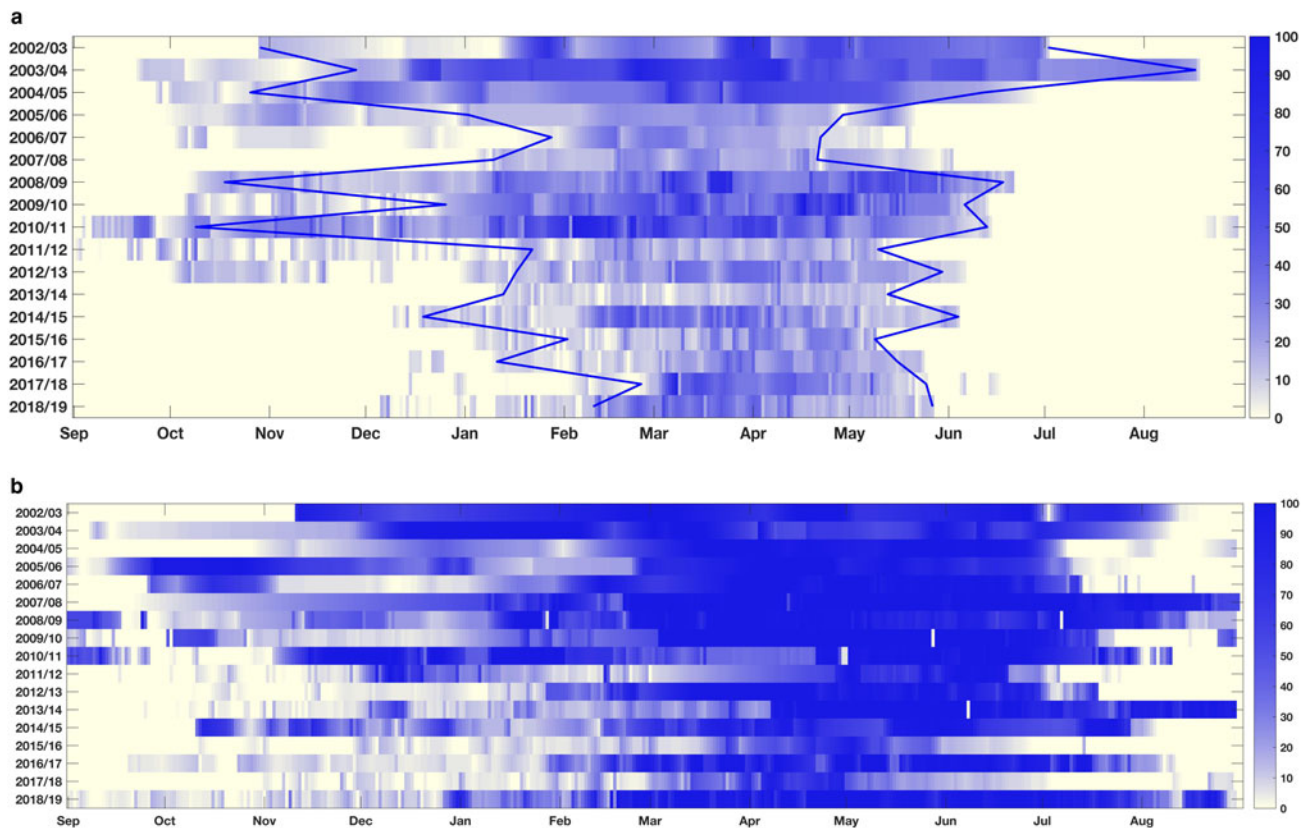
Fig. 9. Total fjord ice coverage (in %) with months on the *x*-axis and the respective sea ice seasons of 2002/03–2018/19 on the *y*-axis for (a) Kongsfjorden and (b) Rijpfjorden. The lowest sea ice cover is generally observed in September and the first day of September is set as the start of the fjord ice season. In (a) the start and the end of the fjord ice season are indicated by two blue lines.

Svalbard and Franz Josef Land. Lind and others (2018) found that since 2003 there has been an overall reduction in the sea ice volume exchange between Svalbard and Franz Josef Land, though yearly fluctuations were also observed. The observed warmer water temperatures and reduced sea ice volume may lead to shorter sea ice seasons in Rijpfjorden or a shift towards a higher proportion of locally formed fast ice within the fjord.

Here we have only looked into the water temperature effect on the fjord ice evolution, further studies should also include atmospheric forcings such as temperature, wind and radiative forcing.

6. Conclusions

We found that the presented classification method, providing a solid base for open water–ice differentiation, is transferable between a range of different SAR sensors and can therefore be used to establish consistent fjord ice records. No systematic differences were observed between the single-channel sensors and the dual-channel sensors. Given the potential advantage of separating wind-roughened open water from sea ice in the cross-polarisation channel we suggest that for long-term sea ice records to utilise both backscatter channels when they are available.

For Kongsfjorden, the identified fjord ice extent corresponds well to manually drawn maps covering the same area and the ice edge corresponds well to the in-situ identified ice edge. The fjord ice areas observed in 10 and 50 m pixel resolution images show a good agreement. From this we conclude that the proposed method can establish robust and reliable fjord ice area records.

Using the fjord ice record we observe that the ice in Kongsfjorden has a reduced surface areal extent, a shorter fjord ice season and that the sea ice is now forming later in the year than at the start of the century. Moreover, there is a good

correlation between the maximum water temperature and the maximum fjord ice areal extent and the stability of the ice. For Rijpfjorden we observe a trend towards shorter fjord ice seasons, possibly a consequence of reduced sea ice north-east of Svalbard and warmer water temperatures. With the expected continuation of the operation of S-1 satellites, it will be possible to extend the fjord ice record into the future.

References

Ambrose W, Carroll M, Greenacre M, Thorrold S and McMahon K (2006) Variation in serripes groenlandicus (bivalvia) growth in a Norwegian high-Arctic fjord: evidence for local- and large-scale climatic forcing. *Global Change Biology* **12**(9), 1595–1607. doi: 10.1111/j.1365-2486.2006.01181.x

Arrigo K and van Dijken G (2015) Continued increases in Arctic Ocean primary production. *Progress in Oceanography* **136**, 60–70. doi: 10.1016/j.pocean.2015.05.002

Assmy P and 40 others (2017) Leads in Arctic pack ice enable early phytoplankton blooms below snow-covered sea ice. *Scientific Reports* **7**(40850). doi: 10.1038/srep40850

Bliss A, Miller J and Meier W (2017) Comparison of passive microwave-derived early melt onset records on arctic sea ice. *Remote Sensing* **9**(199). doi: 10.3390/rs9030199

Collecte Localisation Satellites (2019) *Sentinel-1 Product Specification* (Technical Report S1-RS-MDA-52-7441). European Space Agency.

Cottier F and 5 others (2007) Wintertime warming of an Arctic shelf in response to large-scale atmospheric circulation. *Geophysical Research Letters* **34**(10), L10607. doi: 10.1029/2007GL029948

Cottier F, Skogseth R, David D and Berge J (2019) Temperature time-series in Svalbard fjords. A contribution from the integrated marine observatory partnership (imop). In Orr E (ed), *SESS Report 2018*, Longyearbyen: Svalbard Integrated Arctic Earth Observation System (SIOS). Available at www.sios-svalbard.org/SESSreport.

Cristea A, Van Houtte J and Doulgeris A (undergoing revisions) Integrating incidence angle dependencies into the clustering-based segmentation of SAR images. *IEEE Journal of Selected Topics in Applied Earth Observations and Remote Sensing*.

Doulgeris A and Cristea A (2018) Incorporating incidence angle variation into SAR image segmentation. *IGARSS 2018 - IEEE International Geoscience and Remote Sensing Symposium*. doi: 10.1109/IGARSS.2018.8519043

Dowdeswell J and Forsberg C (1992) The size and frequency of icebergs and bergy bits derived from tidewater glaciers in Kongsfjorden, northwest Spitsbergen. *Polar Research* **11**(2), 81–91. doi: 10.3402/polar.v11i2.6719

Eisenman I, Meier W and Norris J (2014) A spurious jump in the satellite record: has Antarctic sea ice expansion been overestimated?. *The Cryosphere* **8**, 1289–1296. doi: 10.5194/tc-8-1289-2014

Fetterer F, Knowles K, Meier W, Savoie M and Windnagel A (2019) Sea Ice Index, Version 3. Northern Hemisphere Extent Anomalies Aug. 1979–2019. Boulder, Colorado USA. NSIDC: National Snow and Ice Data Center. doi:10.7265/N5K072F8

Garmin (2011) GPSMAP 62 series owners manual. Available at http://static.garmin.com/pumac/GPSMAP62OMEN.pdf.

Gerland S and Renner AHH (2007) Sea ice mass balance in an Arctic fjord. *Annals of Glaciology* **46**, 435–442. doi: 10.3189/172756407782871215

Giles K, Laxon S and Ridout A (2008) Circumpolar thinning of Arctic sea ice following 2007 record ice extent minimum. *Geophysical Research Letters* **35** (22). doi: 10.1029/2008GL035710

Gupta M, Barber D, Scharien RK and Isleifson D (2014) Detection and classification of surface roughness in an Arctic marginal sea ice zone. *Hydrological Processes* **28**, 599–609. doi: 10.1002/hyp.9593

Hop H and 14 others (2019a) Pelagic ecosystem characteristics across the Atlantic water boundary current from Rijpfjorden, Svalbard, to the Arctic Ocean during summer (2010–2014). *Frontiers in Marine Science* **6**(181). doi: 10.3389/fmars.2019.00181

Hop H, Cottier F and Berge J (2019b) Autonomous Marine Observatories in Kongsfjorden, Svalbard (2003–2016). In Hop H and Wiencke C (eds), *The Ecosystem of Kongsfjorden, Svalbard. Advances in Polar Ecology*. Springer Verlag, pp. 515–533. doi: 10.100/978-3-319-46425-1

Howe J and 7 others (2010) Dinoflagellate cysts as proxies for palaeoceanographic conditions in arctic fjords. *Geological Society, London, Special Publications* **344**, 61–74. doi: 10.1144/SP344.6

Isaksen K and 5 others (2016) Recent warming on Spitsbergen - influence of atmospheric circulation and sea ice cover. *Journal of Geophysical Research: Atmospheres* **121**, 11913–11931. doi: 10.1002/2016JD025606

Kwok R and Cunningham C (2015) Variability of Arctic sea ice thickness and volume from CryoSat-2. *Philosophical Transactions of the Royal Society A* **373**(2045). doi: 10.1098/rsta.2014.0157

Larsen Y, Engen G, Lauknes T, Malnes E and Høgda K (2006) A generic differential interferometric SAR processing system, with applications to land subsidence and snow-water equivalent retrieval. In *Fringe 2005 Workshop* (Vol. 610).

Leu E, Graeve M and Wulff A (2016) A (too) bright future? - Arctic diatoms under radiation stress. *Polar Biology* **39**, 1711–1724. doi: 10.1007/s00300-016-2003-1

Leu E, Søreide J, Hessen D, Falk-Petersen S and Berge J (2011) Consequences of changing sea-ice cover for primary and secondary producers in the European Arctic shelf seas: timing, quantity and quality. *Progress in Oceanography* **90**(1–4), 18–32. doi: 10.1016/j.pocean.2011.02.004

Lind S, Ingvaldsen R and Furevik T (2018) Arctic warming hotspot in the northern Barents Sea linked to declining sea-ice import. *Nature Climate Change* **8**, 634–639. doi: 10.1038/s41558-018-0205-y

Lindsay R and Schweiger A (2015) Arctic sea ice thickness loss determined using subsurface, aircraft, and satellite observations. *The Cryosphere* **9**(1), 269–283. doi: 10.5194/tc-9-269-2015

Luckman A and 5 others (2015) Calving rates at tidewater glaciers vary strongly with ocean temperature. *Nature Communications* **6**(8566). doi: 10.1038/ncomms9566

Mahmud MS and 5 others (2018) Incidence angle dependence of HH-polarized C- and L-band wintertime backscatter over Arctic Sea Ice. *IEEE Transactions on Geoscience and Remote Sensing* **56**(11), 6686–6698. doi: 10.1109/TGRS.2018.2841343

Muckenhuber S, Nilsen F, Korosov A and Sandven S (2016) Sea ice cover in Isfjorden and Hornsund, Svalbard (2000–2014) from remote sensing data. *The Cryosphere* **10**, 149–158. doi: 10.5194/tc-10-149-2016

Negrel J, Gerland S, Doulgeris A, Lauknes T and Rouyet L (2018) On the potential of hand-held GPS tracking of fjord ice features for remote sensing validation. *Annals of Glaciology* **59**(76pt2), 173–180. doi: 10.1017/aog.2017.35

Nilsen F, Skogseth R, Vaardal-Lunde J and Inall M (2016) A simple shelf circulation model: intrusion of Atlantic Water on the West Spitsbergen Shelf. *Journal of Physical Oceanography* **46**(4), 1209–1230. doi: 10.1175/JPO-D-15-0058.1

Norwegian Polar Institute (2014) Kartdata Svalbard 1:100 000 (S100 Kartdata) / Map Data [Data set]. Norwegian Polar Institute. doi:10.21334/npolar.2014.645336c7

Norwegian Polar Institute (2019) MOSJ Environmental monitoring of Svalbard and Jan Mayen. Available at http://www.mosj.no/en/climate/ocean/temperature-salinity-fram-strait.html.

Onarheim I, Smedsrud L, Ingvaldsen R and Nilsen F (2014) Loss of sea ice during winter north of Svalbard. *Tellus A* **66**(1), 23933. doi: 10.3402/tellusa.v66.23933

Pavlova O, Gerland S and Hop H (2019) Changes in sea-ice extent and thickness in Kongsfjorden, Svalbard (2003–2016). In Hop H and Wiencke C (eds), *The Ecosystem of Kongsfjorden, Svalbard. Advances in Polar Ecology*. Springer Verlag, pp. 105–136. doi: 10.1007/978-3-319-46425-1

Polyakov I and 15 others (2017) Greater role for Atlantic inflows on sea-ice loss in the Eurasian Basin of the Arctic Ocean. *Science* **356**(6335), 285–291.

Sandven S, Kloster K, Alexandrov V and Piotrovskaya N [Zakhvatkina N] (2008) Sea ice classification using ASAR alternating polarisation images. SeaSAR 2008, 21–24 January 2008, Oslo, Norway.

Schellenberger T, Dunse T, Kääb A, Kohler J and Reijmer C (2015) Surface speed and frontal ablation of Kronebreen and Kongsbreen, NW Svalbard, from SAR offset tracking. *The Cryosphere* **9**, 2339–2355. doi: 10.5194/tc-9-2339-2015

Schild K and 9 others (2018) Glacier calving rates due to subglacial discharge, fjord circulation, and free convection. *Journal of Geophysical Research: Earth Surface* **123**, 2189–2204. doi: 10.1029/2017JF004520

Screen J and Simmonds I (2010) Increasing fall-winter energy loss from the Arctic Ocean and its role in Arctic temperature amplification. *Geophysical Research Letters* **37**(L16707). doi: 10.1029/2010GL044136

Shokr M (2009) Compilation of a radar backscatter database of sea ice types and open water using operational analysis of heterogeneous ice regimes. *Canadian Journal of Remote Sensing* **35**(4), 369–384. doi: 10.5589/m09-026

Søreide J, Leu E, Berge J, Graeve M and Falk-Petersen S (2010) Timing of blooms, algal food quality and calanus glacialis reproduction and growth in a changing Arctic. *Global Change Biology* **16**, 3154–3163.

Stroeve J, Markus T, Boisvert L, Miller J and Barrett A (2014) Changes in Arctic melt season and implications for sea ice loss. *Geophysical Research Letters* **41**(4), 1216–1225. doi: 10.1002/2013GL058951

Stroeve J, Markus T, Meier W and Miller J (2012) The Arctic's rapidly shrinking sea ice cover: a research synthesis. *Climate Change* **110**, 1005–1027. doi: 10.1007/s10584-011-0101-1

Svendsen H and 14 others (2002) The physical environment of Kongsfjorden – Krossfjorden, an Arctic fjord system in Svalbard. *Polar Research* **21**, 133–166. doi: 10.1111/j.1751-8369.2002.tb00072.x

Torsvik T and 7 others (2019) Impact of tidewater glacier retreat on the fjord system: modeling present and future circulation in Kongsfjorden, Svalbard. *Estuarine, Coastal and Shelf Science* **220**, 159–165. doi: 10.1016/j.ecss.2019.02.005

Tverberg V and 8 others 2019) The kongsfjorden transect: seasonal and inter-annual variability in hydrography. In Hop H and Wiencke C (eds), *The Ecosystem of Kongsfjorden, Svalbard. Advances in Polar Ecology*. Springer Verlag, pp. 49–104. doi: 10.1007/978-3-319-46425-1

Wallace M and 5 others (2010) Comparison of zooplankton vertical migration in an ice-free and a seasonally ice-covered Arctic fjord: an insight into the influence of sea ice cover on zooplankton behavior. *Limnology and Oceanography* **55**(2), 831–845.

Wang C and 7 others (2013) Spring sea-ice evolution in Rijpfjorden (80°N), Svalbard, from in situ measurements and ice mass-balance buoy (IMB) data. *Annals of Glaciology* **54**(62), 253–260. doi: 10.3189/2013AoG62A135

Zakhvatkina N, Korosov A, Muckenhuber S, Sandven S and Babiker M (2017) Operational algorithm for ice–water classification on dual-polarized RADARSAT-2 images. *The Cryosphere* **11**(1), 33–46. doi: 10.5194/tc-11-33-2017